ARTICLE

Interfacial Effect induced by Rare Earth Oxide in Boosting Conversion of CO_2 to Formate

Received 00th January 20xx,
Accepted 00th January 20xx

DOI: 10.1039/x0xx00000x

Lianpeng Song,[a] Zhong Liang,[a] Mingzi Sun,[b] Bolong Huang[b,*], Yaping Du[a,*]

The selectivity in the electrocatalysis of carbon dioxide reduction reaction (CO_2RR) has attracted tremendous attention but still faces a great challenge. Constructing the interface becomes an advanced strategy to effectively modulate the electroactivity and selectivity. Herein, we report the synthesis of CeO_2/Bi_3NbO_7 fibrous tubular through a simple electrospinning method, which has shown a much-improved selectivity of 84.73% towards the formic acid with remarkable durability in CO_2RR. Theoretical calculations have demonstrated that the construction interface has supplied highly electroactive regions with efficient electron transfer, which not only improves the adsorption of key adsorbates but also alleviates the reaction energy barriers. The modulation induced by the interface enables the high selectivity and yield of HCOOH. This work has supplied a novel and advanced strategy to utilize the interfacial effect in developing superior CO_2RR electrocatalysts in the future.

Introduction

The global concerns of the ever-growing atmospheric concentration of carbon dioxide (CO_2) have brought to increasing efforts in the storage and conversion of CO_2.[1-2] Electrochemical reduction of CO_2 is an efficient, cost-effective, and environment-friendly method to convert CO_2 into valuable chemical fuels.[3] Although considerable achievements have been made in the improvement of the efficiency of CO_2 reduction reaction (CO_2RR), the selectivity to the single product and the involved reaction mechanisms remain a great challenge.[4] Formic acid, which is of high economic value and high selectivity, has been considered as one of the most ideal reductive products due to its high value for industrial applications.[5] In recent years, several transition metals (Hg, Pb, In, Sn, and Bi) have shown promising electrocatalytic activity for the conversion of CO_2 to formic acid.[6-7] Compared to the other metals, Bi-based materials are non-toxic and inexpensive for large-scale applications. However, the selectivity to formic acid and the critical factors that determine the type of the products still hinder their applications towards the CO_2RR.[8-9] In this case, many attempts have been made to improve the selectivity of Bi-based catalysts.[8-10] For instance, Kourosh Kalantar-Zadeh et al. have demonstrated that alloying can significantly increase the selectivity of Bi_xSn_{1-x} nanoalloy towards HCOOH to 78%.[11] Zeng's group has fabricated Bi@Sn nanoparticles with an increased selectivity of 92% to formic acid, which is much higher than that of the Bi nanoparticles.[12] Despite such inspiring results, the electronic interaction between Bi and the cocatalyst functioned on the selectivity to formic acid has been unclear, as well as the synthetic method is generally complicated, which has limited the development of efficient and practical Bi-based electrocatalysts for the CO_2RR.[11-12] Currently, many different strategies have been proposed to improve the electrochemical performances such as morphology modifications and defect engineering. Besides these approaches, the construction of interface has also been a promising method, especially for the oxide-based electrocatalysts. Cuenya's group has developed the SnO_x/AgO_x electrocatalyst with the facilitation of plasma techniques, which shows 95% Faradic efficiency (FE) for the C_1 products due to the strong suppression of the competing hydrogen evolution reaction (HER) [J. Am. Chem. Soc. 2019, 141, 13, 5261–5266]. The interface formed during the electrochemical tests also benefits the CO_2RR. The in situ reconstruction of hierarchical Sn–Cu/SnO_x core/shell catalyst leads to the optimizations of the binding strength of intermediates. [Angew. Chem. Int. Ed. 59(12), 4814–4821 (2020)]. However, most of the interface engineering works are based on noble metals.

Rare earth oxide such as cerium oxide (CeO_2) has been widely used as the cocatalyst to boost the conversion in various electrochemical reactions due to the rich oxygen vacancy defects and unique electronic structures.[13-17] Very recently, CeO_2 has been demonstrated to be a potential additive in improving the selectivity of Bi and carbon nanotubes, where the selectivity of the formic acid has been increased around 10%.[18-19] To date, the research of incorporating rare earth oxides to further improve the selectivity to formic acid is still limited.

[a] *Tianjin Key Lab for Rare Earth Materials and Applications, Center for Rare Earth and Inorganic Functional Materials, School of Materials Science and Engineering, National Institute for Advanced Materials, Nankai University, Tianjin 300350, China.*
[b] *Department of Applied Biology and Chemical Technology, The Hong Kong Polytechnic University, Hung Hom, Kowloon, Hong Kong SAR, China.*
**Correspondence to: bhuang@polyu.edu.hk; ypdu@nankai.edu.cn*
† Footnotes relating to the title and/or authors should appear here.
Electronic Supplementary Information (ESI) available: [details of any supplementary information available should be included here]. See DOI: 10.1039/x0xx00000x

More importantly, the critical contributions of rare earth oxides in CO_2RR still remain ambiguous.

As an electrocatalyst with high selectivity to formic acid, [20-21] we have selected bismuth niobate (Bi_3NbO_7) as a promising candidate to construct the interface with CeO_2 to realize efficient CO_2RR. In this work, through a simple electrospinning method followed by annealing, we have successfully synthesized the homogeneous CeO_2/Bi_3NbO_7 fiber tubular as shown in **Scheme 1**. The obtained electrocatalyst has shown an enhanced selectivity of 84.73% to formic acid, nearly 30% above that of Bi_3NbO_7, and exhibits extraordinary durability in CO_2RR. Density functional theory (DFT) calculations have revealed the introduction of CeO_2 has strongly optimized the electron transfer efficiency by the Ce-4f orbitals and activation of O-orbitals. Such electronic structures have guaranteed the much-improved reaction trend towards the formation of HCOOH and suppressed the CO formation. More importantly, our method has supplied a simple method for the large-scale production of efficient interfacial electrocatalysts when compared to conventional synthesis methods. This work has supplied a deeper understanding of the interfacial effect, which benefits the future design of efficient electrocatalysts for broad applications.

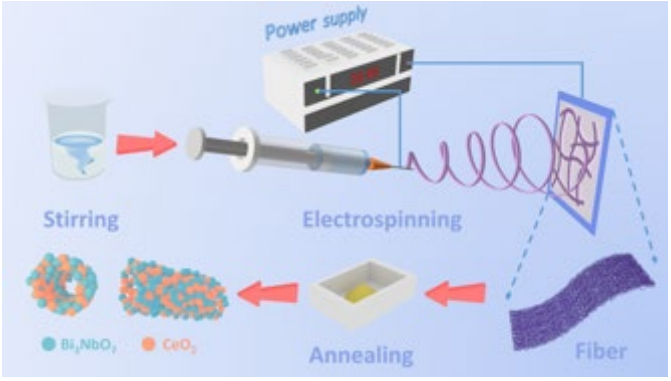

Scheme 1. Schematic illustration of the synthesis of CeO_2/Bi_3NbO_7.

Results and Discussions

CeO_2/Bi_3NbO_7 fiber tubular was synthesized by reacting $Bi(NO_3)_3{\cdot}5H_2O$, $Ce(NO_3)_3{\cdot}6H_2O$, and $C_{10}H_5NbO_{20}$ with an electrospinning method, followed by annealing at 550 °C for 30 minutes. As shown in Fig. S1, the uniform fiber precursor was firstly regulated through a needle with a diameter of 1.20 mm. After calcination, the product showed several weak characteristic peaks corresponding to CeO_2 and Bi_3NbO_7, as shown in **Fig. 1a**, which suggested the crystallinity of the sample has been decreased.[22-23] CeO_2 and Bi_3NbO_7 were comparatively obtained through a similar procedure with different reactants, which showed typical characteristic peaks corresponding to CeO_2 and Bi_3NbO_7, respectively (Fig. S2a-b). Obviously, CeO_2/Bi_3NbO_7, CeO_2, and Bi_3NbO_7 showed similar fiber tubular shapes with diameters of about 150 nm (Fig. 1b, Fig. S3a-b), where the surface of CeO_2/Bi_3NbO_7 was more undulating than that of CeO_2 and Bi_3NbO_7 (Fig. 1c-d, S3a-b). This increases the electrochemical surface area of CeO_2/Bi_3NbO_7.[23] The selected area electron diffraction (SAED) of CeO_2/Bi_3NbO_7 showed two obvious diffraction rings, corresponding to (111) and (200) lattice plane of CeO_2/Bi_3NbO_7 (Fig. 1e). The high-resolution TEM (HRTEM) image of CeO_2/Bi_3NbO_7 showed the lattice spacing of 0.312 and 0.323 nm, corresponding to the (111) lattice plane of CeO_2 and Bi_3NbO_7, respectively (Fig. 1f). The HRTEM images of CeO_2 and Bi_3NbO_7 shown in Fig. S4a-b further indicated the lattice spacing of 0.313 and 0.323 nm were corresponding to the (111) lattice plane of CeO_2 and Bi_3NbO_7, respectively. It is worth noting that the complexes with different spatial structures exhibit different atomic arrangements on both sides of the heterogeneous interface. Even near the interface between the two components, the fringes coherently contacted near the interface are not significantly distorted (Fig. 1f).[24] The unique spatial configuration of CeO_2/Bi_3NbO_7 also shows that there is intimate atomic coupling across the interface between CeO_2 and Bi_3NbO_7, confirming the electronic modulations induced by the interfacial effect (Fig. 1g). In addition, the energy dispersive X-ray spectroscopy (EDS) mapping of CeO_2/Bi_3NbO_7 suggested Bi, Nb, Ce and O were evenly distributed in the whole sample (Fig. 1h-k). For the comparison samples, the Bi, Nb and O were well-distributed in Bi_3NbO_7 (Fig. S5a-d) as well as the Ce and O in CeO_2 (Fig. S6a-c).

The X-ray photoelectron spectroscopy (XPS) measurement was applied to investigate the electron interactions between the elements. As presented in **Fig. 2a**, Bi *4f* of Bi_3NbO_7 and CeO_2/Bi_3NbO_7 both showed one pair of spin-orbit-doublets corresponding to Bi $4f_{5/2}$ and Bi $4f_{7/2}$.[25] Notably, the Bi^{3+} peaks of CeO_2/Bi_3NbO_7 at 158.8 and 164.15 eV were negatively shifted by 0.15 eV compared to Bi^{3+} peaks of Bi_3NbO_7 at 158.95 and 164.3 eV, indicating the electron transfer from CeO_2 to Bi.[26] Interestingly, compared with the Bi_3NbO_7 peaks at 206.5 and 209.2 eV, the CeO_2/Bi_3NbO_7 peaks assigned to Nb^{5+} remain unchanged at 206.5 and 209.2 eV (Fig. 2b), suggesting that electron transfer does not occur between Nb and CeO_2.[26-27] As expected, in Ce *3d* spectra, three pairs of fitted peaks (U, U_1, U_2, U', U_1' and U_2') can be assigned to Ce^{4+}, another one pair of fitted peaks (V and V ') can be presented by Ce^{3+} (Fig. 2c). The negative shift of the fitting peak of lower valence Ce also proves that electrons tend to be pulled by Bi. The proportion of Ce^{3+} in CeO_2/Bi_3NbO_7 (24%) is significantly increased compared to CeO_2 (20%), this may be due to the higher concentration of oxygen vacancies that help balance the charge distribution in the heterostructures.[24] The O *1s* spectra could be divided into O_{surf} at 532.0-533.1 eV for surface-adsorbed H_2O, O_{ads} at 531.1-531.5 eV for oxygen species adsorbed on the surface and O_{latt} at 529.3-529.7 eV for lattice oxygen bonding with metal.[28] Since the dissociative molecular oxygen is adsorbed on the surface oxygen vacancies, the relative content of O_{ads} is closely related to the oxygen vacancies, the relative content of O_{ads} in CeO_2/Bi_3NbO_7 increased from 22% to 29% in Bi_3NbO_7 (Fig. 2d), demonstrating that introduction of CeO_2 does help enrich the oxygen vacancies. This also coincides with the ratio changes of Ce^{3+}/Ce^{4+} in the Ce *3d* spectra (Fig. 2c).[24, 29] Thermogravimetric

analysis (TGA) is employed to explore the oxygen vacancies in Bi_3NbO_7 and CeO_2/Bi_3NbO_7 from another perspective. The larger mass difference of the CeO_2/Bi_3NbO_7 in air and argon indicates more oxygen vacancies (Fig. S7), which is consistent with the XPS analysis.[30, 31]

of Ce/Bi is 1/4, it will obtain the highest efficiency of 75-85% for formate at all selected potentials, while Bi_3NbO_7 only showed $FE_{(HCOOH)}$ of 45-55% at the same potentials. Unexpectedly, HCOOH could not be detected with pure CeO_2 catalyst in the CO_2RR due to the dominating HER.[32] Meanwhile, with the change of Ce mole ratio, although the XRD and morphology of

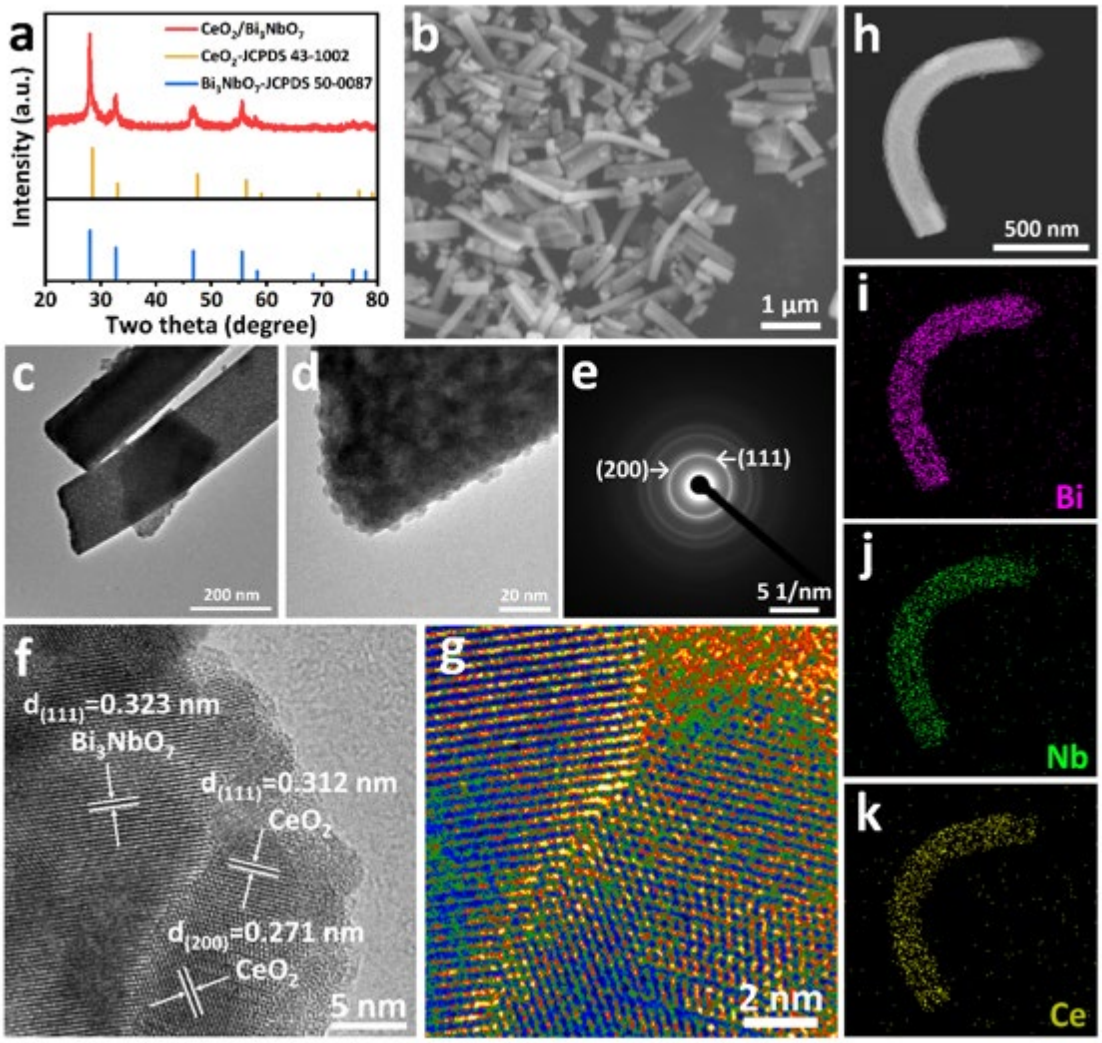

Figure 1. Structural characterizations of CeO_2/Bi_3NbO_7. (**a)** XRD pattern, (**b)** SEM image, (**c)** TEM image, (**d)** magnified TEM image, (**e)** SAED pattern and (**f)** HRTEM image and (**g)** enlarged view of interface and (**h-k)** corresponding elemental mapping images of CeO_2/Bi_3NbO_7.

The CO_2RR performances of all the samples were evaluated by the linear sweep voltammetry (LSV) curves in a CO_2 saturated 0.1M $KHCO_3$ solution and the reaction is carried out in the H-type electrolytic cell (Fig. S8). As shown in **Fig. 3a**, the current density of CeO_2/Bi_3NbO_7 and Bi_3NbO_7 were much higher than that of CeO_2 and blank carbon paper in the whole test range of voltage, indicating Bi_3NbO_7 are more efficient than CeO_2 in the CO_2RR.[32] Notably, the Tafel plot of CeO_2/Bi_3NbO_7 (436 mV dec^{-1}) is much lower than that of Bi_3NbO_7 (602 mV dec^{-1}), suggesting faster reaction kinetics (Fig. S9).[18] The selectivity of Bi_3NbO_7, CeO_2, and CeO_2/Bi_3NbO_7 was determined through the Faradaic efficiency (FE) of CO, H_2 and HCOOH, ^1H Nuclear Magnetic Resonance (NMR) spectroscopy shows no other liquid products except formate (Fig. S10).[18] As shown in Fig. 3b-f, when the ratio

the CeO_2/Bi_3NbO_7 did not change significantly, the FE(HCOOH) has decreased to varying degrees, indicating that the optimal ratio of Ce/Bi is 1/4 (Fig. S11-14). As a result, CeO_2/Bi_3NbO_7 even showed a higher current density of HCOOH (j_{HCOOH}) than that of Bi_3NbO_7 at the whole range of test potential (Fig. 3g), despite the smaller total current density at potential below 1.2 V. The electrochemical impedance spectra (EIS) were employed to explore the charge and mass transfer between the catalysts and the electrolyte. As the Nyquist plots shown in Fig. S15, Bi_3NbO_7 had the smallest charge and mass transfer with semicircle radius of 7.189 Ω at the low frequency region, while CeO_2/Bi_3NbO_7 showed similar semicircle radius of 9.796 Ω, much smaller than CeO_2, indicating a faster charge/mass transfer of Bi_3NbO_7 compared to CeO_2.[21] The electrochemical

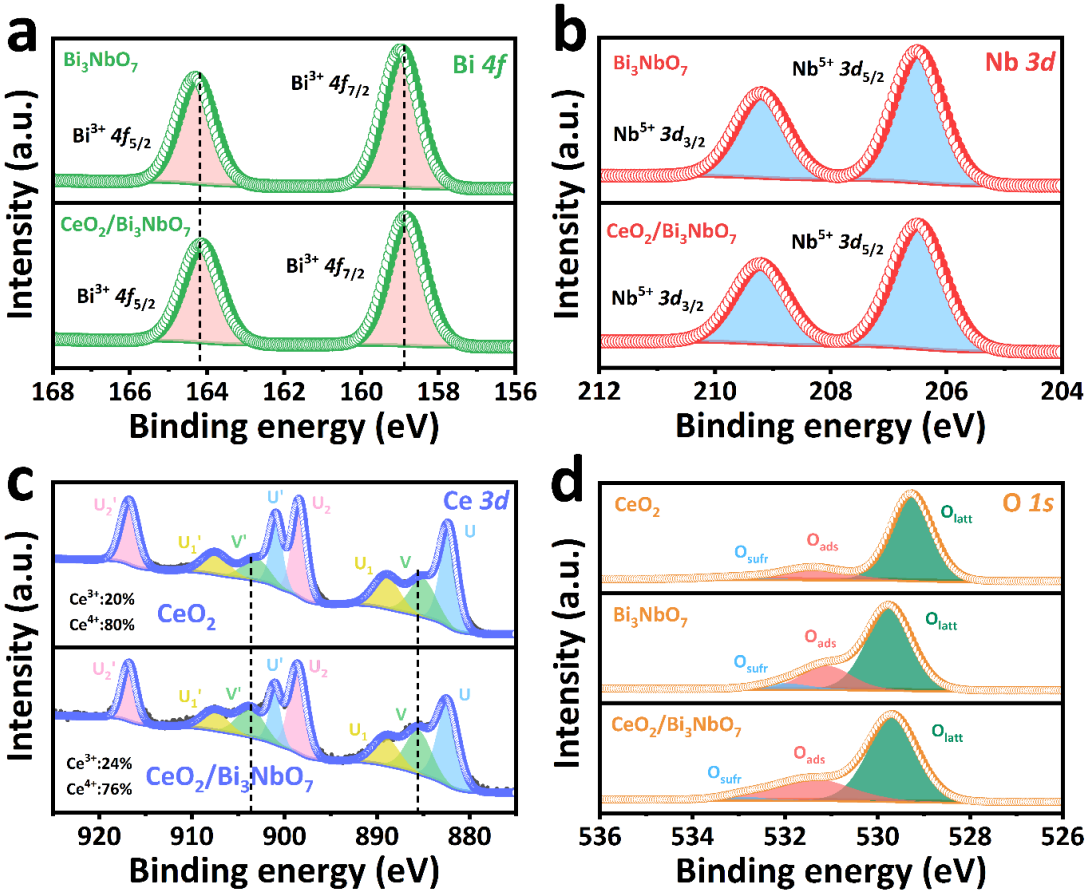

Figure 2. Electronic structural characterizations of CeO_2/Bi_3NbO_7. (a) Bi *4f* spectra of Bi_3NbO_7 and CeO_2/Bi_3NbO_7. (**b**) Nb *3d* spectra of Bi_3NbO_7 and CeO_2/Bi_3NbO_7. (**c**) Ce *3d* XPS spectra of CeO_2 and CeO_2/Bi_3NbO_7. (**d**) O *1s* XPS spectra of CeO_2, Bi_3NbO_7 and CeO_2/Bi_3NbO_7.

surface area (ECSA) of catalysts, which are applied to evaluate the intrinsic activity of the active site, were calculated through the double-layer capacitance (C_{dl}).[33] Cyclic voltammetry (CV) curves of the samples with different scanning rates at open circuit voltage are shown in Fig. S16. The current density differences (Δj) plotted against scanning rates suggested CeO_2/Bi_3NbO_7 possessed a larger ECSA than that of CeO_2. Compared to Bi_3NbO_7, the crystallinity of CeO_2/Bi_3NbO_7 has been decreased, resulting in more oxygen vacancies and active sites exposed. This makes the ECSA of CeO_2/Bi_3NbO_7 close to that of Bi_3NbO_7.[21] Chronoamperometry curve (Fig. 3h) showed the current density was no obvious change after 6-hour-test, suggesting high long-term durability of CeO_2/Bi_3NbO_7 toward CO_2RR at the potential of -1.2 V in 0.1 M $KHCO_3$ solution. During the stability test, 200 µL liquid sample is taken out for testing NMR at the same time interval, and the result showed that the FE of HCOOH has been maintained at around 85%. After that, the sample was vacuum dried and tested again, the results showed that the current density and the FE of HCOOH basically recovered. It is proved by SEM that after a long-term stability test, the morphology of the sample hardly changes significantly (Fig. S17-18).

To investigate the CO_2RR performances, we have further applied the DFT calculations to understand the interfacial induced electronic modulations on CeO_2/Bi_3NbO_7. For the pristine Bi_3NbO_7, the electronic distribution near the Fermi level (E_F) is mainly dominated by Bi and O sites (**Fig. 4a**). The anti-bonding orbitals are mostly contributed by both Bi and Nb sites. With the formation of interface with CeO_2, the electronic structures are strongly affected due to the evident distortions are caused near the interface, which leads to the modulation of the selectivity (Fig. 4b). Moreover, the interface region displays the electron-rich feature to supply an efficient electron transfer pathway. To further reveal the electronic structure, the projected partial density of states (PDOS) are compared between Bi_3NbO_7 and CeO_2/Bi_3NbO_7 (Fig. 4c-d). In Bi_3NbO_7, we notice that the O-2p are dominant near the valence band maximum (VBM) while Nb-4d and Bi-6p orbitals show slightly deeper occupations. On the other side, both Bi-6p and Nb-4d orbitals are the main contributions for the conduction band minimum (CBM), which shows a bandgap of 1.96 eV. In comparison, the formation of the interface significantly changes the electronic structure of CeO_2/Bi_3NbO_7. Notably, the Nb-4d and Bi-6p orbitals have been further suppressed to deeper positions by both O-2p and Ce-4f orbitals. The CBM is mainly constructed by Bi-6p, Nb-4d, and Ce-4f orbitals. Notably, the introduction of Ce-4f orbitals has compensated the barriers from VBM to CBM, which largely promotes the electron transfer on the surface of CeO_2/Bi_3NbO_7, leading to improved faradic

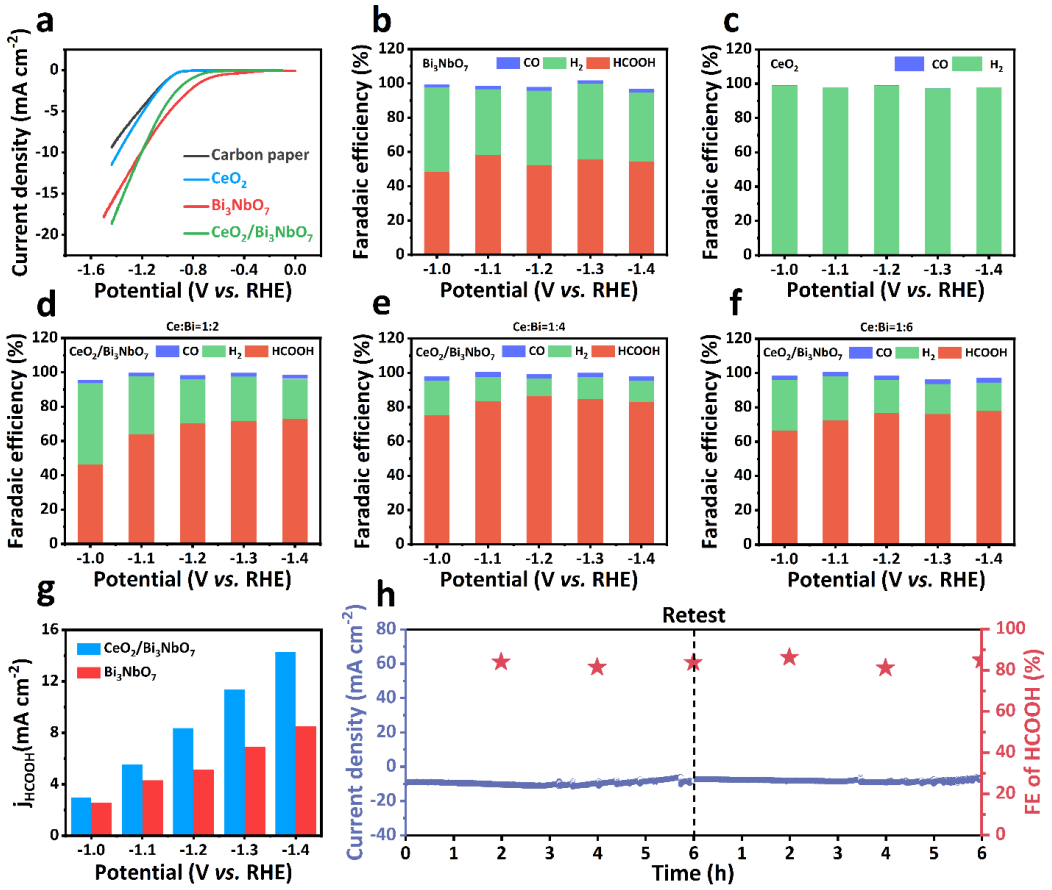

Figure 3. CO_2RR performances characterizations. (a) LSV curves of the CeO_2, Bi_3NbO_7, CeO_2/Bi_3NbO_7 and blank carbon paper. (**b-c)** FE of formic acid, CO_2 and H_2 of Bi_3NbO_7 and CeO_2. **(d-f)** FE of formic acid, CO_2 and H_2 at selected voltages for CeO_2/Bi_3NbO_7 with different molar ratios of Ce and Bi. **(g)** Current density of Bi_3NbO_7 and CeO_2/Bi_3NbO_7 corresponding to $HCOO^-$. **(h)** Chronoamperometry (purple line) and FE of formic acid (red dots) of CeO_2/Bi_3NbO_7 in the -1.2 V (vs RHE).

efficiency towards HCOOH formation. The Nb-4d orbitals in CeO_2/Bi_3NbO_7 are evidently different from the Nb metals and NbO (Fig. 4e). From the bulk to the surface near the interface with CeO_2, the Nb-4d orbitals have shown a downshifting trend, which facilitates the adsorption of CO_2 and other intermediates. For Bi-6p orbitals, we notice that the Bi-6p orbitals near the interface have been significantly activated due to the much-increased electron density near E_F than other Bi sites in the Bi_3NbO_7 component (Fig. 4f). From the bulk to the surface, the introduction of Ce-4f orbitals near VBM enables the alleviation of the energy barrier for electron transfer (Fig. 4g). In addition, the high electron density near the E_F supplies an efficient electron depletion pathway towards the intermediates from CeO_2/Bi_3NbO_7. The O-2p orbitals demonstrate a similar upshifting trend from bulk to the surface in both CeO_2 and Bi_3NbO_7 components, which indicates the improved electroactivity of the surface O sites (Fig. 4h). Meanwhile, for the interface region, the O-2p orbitals exhibit the broadened characteristic on the surface, which strengthens the orbital coupling with intermediate species to facilitate the CO_2RR process. The s,p orbitals of key adsorbates have been demonstrated on CeO_2/Bi_3NbO_7 (Figure 4i). The conversion from CO_2 to HCOOH delivers a highly linear correlation, supporting the efficient electron transfer with low barriers. The deviation of the PDOS of COOH* leads to unfavored selectivity with an increased barrier for electron transfer. From the energetic perspective, the adsorption of the CO_2 and CO show a highly distinct preference (Fig. 4j). Although CO_2 is both spontaneously adsorbed on Bi_3NbO_7 and CeO_2/Bi_3NbO_7, the much stronger preference of CO binding leads to weakened selectivity towards HCOOH on Bi_3NbO_7. Then, the reaction energy changes for both HCOOH and CO formation are compared on pristine Bi_3NbO_7 and CeO_2/Bi_3NbO_7 (Fig. 4k). For the HCOOH formation, although both Bi_3NbO_7 and CeO_2/Bi_3NbO_7 show the overall energetically favored reaction, the energy barrier of 0.17 eV on Bi_3NbO_7 strongly hinders the formation of HCOOH while the spontaneous reaction trend of CeO_2/Bi_3NbO_7 guarantees the high selectivity towards HCOOH. For the CO formation, the large energy barrier of COOH* formation on CeO_2/Bi_3NbO_7 suppresses the CO formation as experimental results (Fig. 4l). For the pristine Bi_3NbO_7, the selectivity towards CO is stronger due to the spontaneous reaction trend.

Conclusions

In conclusion, we have constructed a novel electrocatalytic composite CO_2RR catalyst composed of CeO_2 and Bi_3NbO_7. The single selection performance of this material for formic acid reaches 85% and exhibits long-term stability. CeO_2 plays a vital

role as the trigger, the introduction of CeO_2 could reduce the crystallinity of material and significantly change electron interactions and coordination environment to activate the CO_2RR active site of Bi_3NbO_7, increasing dramatically the yield of HCOOH. DFT calculations have indicated that the existence of the CeO_2/Bi_3NbO_7 interface has activated the surface electroactivity. Due to the introduction of Ce-4f orbitals, the energy barrier of electron transfer has been significantly reduced, leading to the improved electroactivity and reaction trend towards the formation of HCOOH. This work will provide a new strategy for the extended applications of rare earth oxides and the design of highly efficient electrocatalysts for CO_2RR.

Experiments

Chemicals. Niobium (V) oxalate hydrate ($C_{10}H_5NbO_{20}{\cdot}xH_2O$, 98.0%, Energy Chemical), Bismuth (III) nitrate pentahydrate ($Bi(NO_3)_3{\cdot}5H_2O$, 99.0%, Aladdin), Cerium (III) nitrate hexahydrate ($Ce(NO_3)_3{\cdot}6H_2O$, 99.0%, Aladdin), Citric acid ($C_6H_8O_7$, ≥ 99.5%, Macklin), N, N-dimethylformamide ($HCON(CH_3)_2$, ≥ 99.5%, Damao), Acetate ($C_2H_4O_2$, ≥ 99.9%, Macklin), Polyvinylpyrrolidone ($(C_6H_9NO)_n$, MW ≈ 1300000, Aladdin) and Ethanol (C_2H_6O, 95%, Tianjin Concord Technology).

Synthesis of CeO_2/Bi_3NbO_7. Typically, 0.728 g $Bi(NO_3)_3{\cdot}5H_2O$ and 0.25 g Citric acid dissolved in 8 mL DMF, then 1 mL of Acetate was added into the solution with stirring at room temperature. After the solid powder dissolved, 0.163 g $Ce(NO_3)_3{\cdot}6H_2O$ and 0.269 g Niobium oxalate hydrate was added into the solution, after that, 4 mL Ethanol was added slowly into the above solution. A certain amount of Polyvinylpyrrolidone was added into the dispersion after mixing well. The precursor sols were obtained after continuous stirring for 12 h at room temperature. The sols were drawn into a syringe with a needle diameter of 1.20 mm, and then the precursor sols were subsequently electrospinning at a constant flow rate of 0.4 mL h^{-1} and at a high voltage of 16 kV, the distance between the injector needle and the receiver was 16 cm. After drying at 60 °C for 12 h in the vacuum oven, the as-spun fibers were transferred

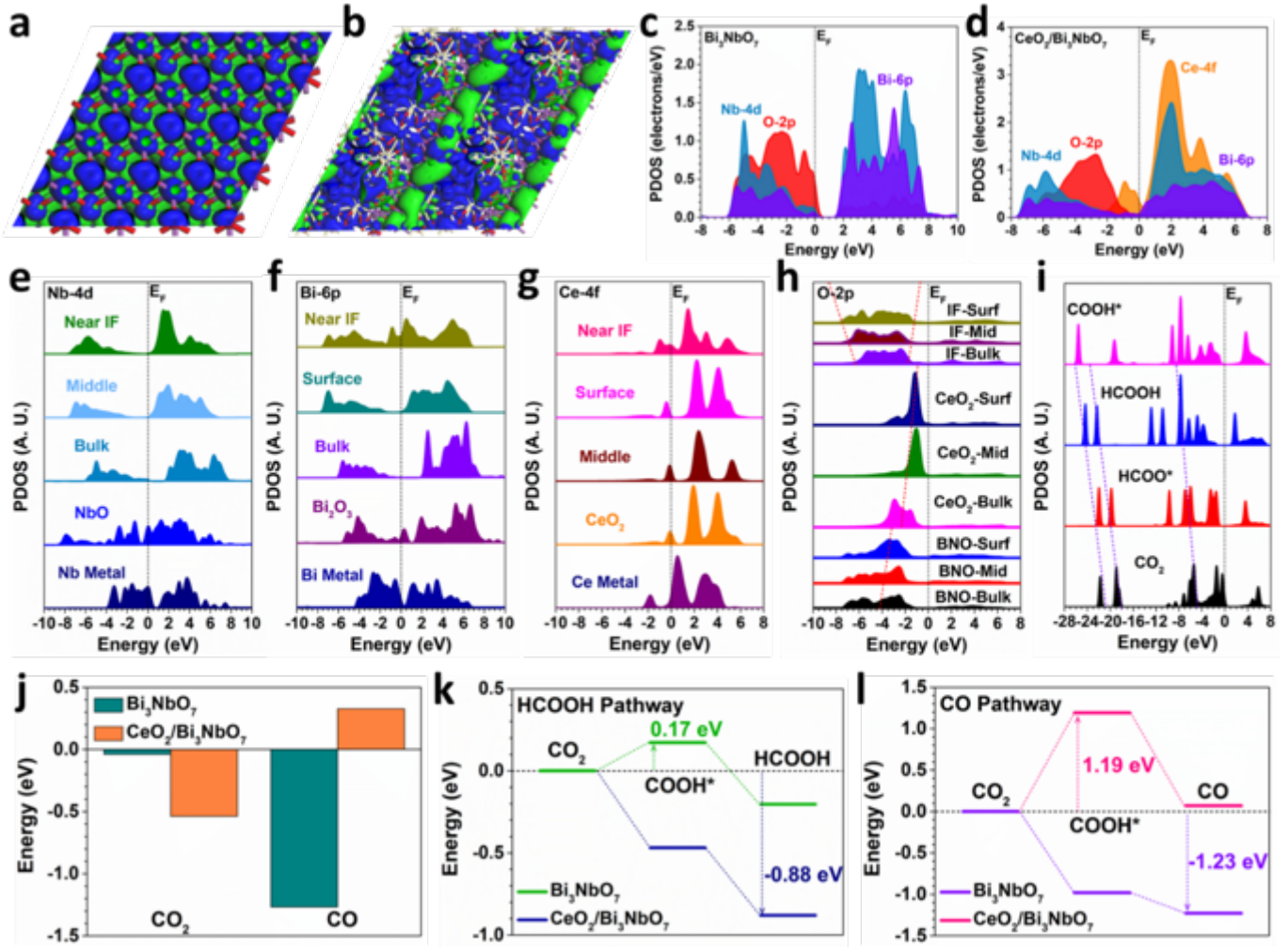

Figure 4. DFT calculations. The 3D contour plot of electronic distribution near Fermi level of **(a)** Bi_3NbO_7 and **(b)** CeO_2/Bi_3NbO_7. Purple balls= Bi, Cyan balls = Nb, Yellow balls = Ce and Red balls = O. Blue Isosurface = bonding orbitals and green isosurface = anti-bonding orbitals. The PDOS comparison of **(c)** Bi_3NbO_7 and **(d)** CeO_2/Bi_3NbO_7. The site-dependent PDOS of **(e)** Nb-4d, **(f)** Ce-4f, **(g)** Bi-6p and (h) O-2p. **(i)** The PDOS comparison of key adsorbates in CO_2RR towards HCOOH on CeO_2/Bi_3NbO_7. **(j)** The adsorption energies of CO_2 and CO on Bi_3NbO_7 and CeO_2/Bi_3NbO_7. The reaction trend of **(k)** HCOOH and **(l)** CO reaction pathways on Bi_3NbO_7 and CeO_2/Bi_3NbO_7.

to the muffle furnace for calcination 550 °C for 30 minutes at a heating rate of 1 °C per minute.

Synthesis of Bi_3NbO_7. Pure Bi_3NbO_7 was synthesized without $Ce(NO_3)_3{\cdot}6H_2O$.
Synthesis of CeO_2. Pure CeO_2 was synthesized without $Bi(NO_3)_3{\cdot}5H_2O$ and Niobium oxalate hydrate.

Material Characterization. Powder X-ray diffraction (XRD) patterns were obtained by a Rigaku Smart Lab Power X-ray diffractometer with Cu Kα source. Data were collected in the 2θ range of 20 – 80 ° at a scanning rate of 4 ° min^{-1}. Transmission electron microscopy (TEM) images, energy-dispersive spectroscopy (EDS) images, and selected area electron diffraction images (SAED) were obtained on a transmission electron microscopy of JEOL JEM-2800 with an acceleration voltage of 200 kV. Scanning electron microscope (SEM) images were acquired on a FESEM JEOL JSM-7800F with an acceleration voltage of 15 kV. X-ray photoelectron spectroscopy (XPS) spectra were performed on a Thermo Scientific ESCALAB 250Xi electron spectrometer with Al Kα radiation. The gas product was detected by the gas chromatograph (GC) of Shimadzu GC 2014C. The liquid product was identified to only contain formic acid by ^{1}H nuclear magnetic resonance (NMR) spectroscopy of Bruker Ascend TM 400.

*Electrochemical measurements***.** All electrochemical measurements were performed with the electrochemical workstation (CHI660E, Chenhua, shanghai) in a three-electrode system. In general, Ag/AgCl electrode was used as the reference and Platinum as the counter electrode. The 5 mg catalyst were dispersed in 240 μL ethylene glycol and 240 μL ethanol as the suspension, 20 μL Nafion was added as a binder. The dispersion was measured 20 μL by pipette drop it evenly on the carbon paper (1 cm × 2 cm) after ultrasound at room temperature 30 minutes. In the CO_2RR experiment, all the reactions were carried out in a H-type electrochemical cell with ion exchange membrane (Nafion, 117) separation between the two cells. 30 mL aqueous solutions of 0.1 M $KHCO_3$ (99.5%, Macklin) as the electrolyte purged with CO_2 for 30 minutes until the solution is saturated, the pH of electrolyte was 6.98. Electrode potentials were converted to the reversible hydrogen electrode (RHE) by the followed equation:

$$E_{RHE} = E_{Ag/AgCl} + 0.197\,V + 0.059 \times pH$$

Product calculation. In this experiment, CO_2 were purged with 20 mL per minute detected by an electronic mass flowmeter. The gas composition was analysis every ten minutes, each CO_2RR catalytic reaction is carried out at different voltages for one hour, we select the test data of the last ten minutes of each hour as the gas composition under this voltage. With the gas composition and proportion, the Faraday efficiency (FE, %) of the gas produced by the CO_2RR process can be calculated the following formula:

$$FE_{gas} = \frac{Q_{gas}}{Q_{tatal}} \times 100\% = \frac{n_{gas} \times v \times t \times F \times N}{V \times Q_{tatal}} \times 100\%$$

Where the n_{gas} is the ppm of gas product (mainly CO and H_2), v is the gas flow rate (20 mL min^{-1}), t is the reaction time as 60 minutes, F represent the faraday constant as 96485 C mol^{-1}, N stands for the number of transferred electrons formed a single molecule of gas (mainly gas of CO and H_2, N = 2), V is the volume of 1 mol gas at 298.15 K and 101.325 kPa, as 24.45 L. Q_{tatal} can be read from the electrochemical workstation.

For the liquid product, the yield of formic acid product was detected by NMR. 200 μL aqueous solutions of electrolyte was measured and added to the NMR tube, 200 μL D_2O (with 1 mmol Sodium acetate anhydrous (CH_3COONa, 99.0%, Macklin) as the internal standard) was mixed into the NMR tube. The FE of the formic acid can be calculated with the performed formula:

$$FE_{liquid} = \frac{Q_{liquid}}{Q_{tatal}} \times 100\% = \frac{n_{liquid} \times F \times N}{Q_{tatal}} \times 100\%$$

Where the n_{liquid} is the amount of substance of the produced formic acid, F also represents the faraday constant as 96485 C mol^{-1}, N stands for the number of transferred electrons generate by one formic acid molecule (N = 2 also).

Calculation Setup. To investigate the CO_2RR performances of the CeO_2/Bi_3NbO_7, we selected the DFT calculations within the CASTEP packages to perform the theoretical calculations regarding both electronic structures and energetic preference.[34] For the functionals, the generalized gradient approximation (GGA) and Perdew-Burke-Ernzerhof (PBE) functionals have been chosen since they are able to supply accurate descriptions of exchange-correlation interactions.[35-37] Based on the convergence tests, we have set the plane-wave basis cutoff energy to 380 eV and selected the ultrasoft pseudopotentials to guarantee the accuracy of the geometry optimizations. Meanwhile, we have applied the Broyden-Fletcher-Goldfarb-Shannon (BFGS) algorithm[38] and selected the coarse quality setting for the k-points during the energy minimizations. To guarantee the geometry relaxations, we have introduced 20 Å vacuum space in the z-axis for all the models. For the geometry optimizations, the following criteria have been used to achieve sufficient relaxation: the Hellmann-Feynman forces should be smaller than 0.001 eV/Å, the total energy difference should not exceed 5×10^{-5} eV/atom, and the inter-ionic displacement should be less than 0.005 Å.

Author Contributions

B. Huang and Y. Du conceived and supervised the research. L. Song and Y. Du designed the experiments. Y. Du, L. Song, and Z. Liang participated in the experimental data analyses and discussions. M. Sun and B. Huang performed the DFT simulations. All authors discussed the results and the preparation of the manuscript.

Conflicts of interest

There are no conflicts to declare.

Acknowledgements

We gratefully acknowledge the financial support from the National Key R&D Program of China (2021YFA1501101), National Natural Science Foundation of China (21971117, 21771156), Functional Research Funds for the Central Universities, Nankai University (63186005), Tianjin Key Lab for Rare Earth Materials and Applications (ZB19500202), the Open Funds (No. RERU2019001) of the State Key Laboratory of Rare Earth Resource Utilization, the National Key R&D Program of China (No. 2017YFA0208000), 111 Project (No. B18030) from China, the Outstanding Youth Project of Tianjin Natural Science Foundation (20JCJQJC00130), the Key Project of Tianjin Natural Science Foundation (20JCZDJC00650), the NSFC/RGC Joint Research Scheme Project (N_PolyU502/21), and the funding for Projects of Strategic Importance of The Hong Kong Polytechnic University (Project Code: 1-ZE2V).

References

1 Nitopi, S.; Bertheussen, E.; Scott, S. B.; Liu, X.; Engstfeld, A. K.; Horch, S.; Seger, B.; Stephens, I. E. L.; Chan, K.; Hahn, C.; Norskov, J. K.; Jaramillo, T. F.; Chorkendorff, I. Progress, and Perspectives of Electrochemical CO_2 Reduction on Copper in Aqueous Electrolyte. *Chem Rev* **2019,** *119* (12), 7610-7672.

2 Zhang, S.; Saji, S. E.; Yin, Z.; Zhang, H.; Du, Y.; Yan, C. H. Rare-Earth Incorporated Alloy Catalysts: Synthesis, Properties, and Applications. *Adv Mater* **2021,** *33* (16), e2005988.

3 Zheng, Y.; Vasileff, A.; Zhou, X.; Jiao, Y.; Jaroniec, M.; Qiao, S. Z. Understanding the Roadmap for Electrochemical Reduction of CO_2 to Multi-Carbon Oxygenates and Hydrocarbons on Copper-Based Catalysts. *J Am Chem Soc* **2019,** *141* (19), 7646-7659.

4 Birdja, Y. Y.; Pérez-Gallent, E.; Figueiredo, M. C.; Göttle, A. J.; Calle-Vallejo, F.; Koper, M. T. M. Advances and challenges in understanding the electrocatalytic conversion of carbon dioxide to fuels. *Nat Energy* **2019,** *4* (9), 732-745.

5 Bagger, A.; Ju, W.; Varela, A. S.; Strasser, P.; Rossmeisl, J. Electrochemical CO_2 Reduction: A Classification Problem. *Chemphyschem* **2017,** *18* (22), 3266-3273.

6 Han, N.; Ding, P.; He, L.; Li, Y.; Li, Y. Promises of Main Group Metal–Based Nanostructured Materials for Electrochemical CO_2 Reduction to Formate. *Adv Energy Mater* **2019,** *10* (11), 1902388.

7 Wen, G.; Lee, D. U.; Ren, B.; Hassan, F. M.; Jiang, G.; Cano, Z. P.; Gostick, J.; Croiset, E.; Bai, Z.; Yang, L.; Chen, Z. Orbital Interactions in Bi-Sn Bimetallic Electrocatalysts for Highly Selective Electrochemical CO_2 Reduction toward Formate Production. *Adv Energy Mater* **2018,** *8* (31), 1802327.

8 Han, N.; Wang, Y.; Yang, H.; Deng, J.; Wu, J.; Li, Y.; Li, Y. Ultrathin bismuth nanosheets from in situ topotactic transformation for selective electrocatalytic CO_2 reduction to formate. *Nat Commun* **2018,** *9* (1), 1320.

9 Zhang, T.; Qiu, Y.; Yao, P.; Li, X.; Zhang, H. Bi-Modified Zn Catalyst for Efficient CO_2 Electrochemical Reduction to Formate. *ACS Sustainable Chem & Eng* **2019,** *7* (18), 15190-15196.

10 Gong, Q.; Ding, P.; Xu, M.; Zhu, X.; Wang, M.; Deng, J.; Ma, Q.; Han, N.; Zhu, Y.; Lu, J.; Feng, Z.; Li, Y.; Zhou, W.; Li, Y. Structural defects on converted bismuth oxide nanotubes enable highly active electrocatalysis of carbon dioxide reduction. *Nat Commun* **2019,** *10* (1), 2807.

11 Xing, Y.; Kong, X.; Guo, X.; Liu, Y.; Li, Q.; Zhang, Y.; Sheng, Y.; Yang, X.; Geng, Z.; Zeng, J. Bi@Sn Core-Shell Structure with Compressive Strain Boosts the Electroreduction of CO2 into Formic Acid. *Adv Sci (Weinh)* **2020,** *7* (22), 1902989.

12 Tang, J.; Daiyan, R.; Ghasemian, M. B.; Idrus-Saidi, S. A.; Zavabeti, A.; Daeneke, T.; Yang, J.; Koshy, P.; Cheong, S.; Tilley, R. D.; Kaner, R. B.; Amal, R.; Kalantar-Zadeh, K. Advantages of eutectic alloys for creating catalysts in the realm of nanotechnology-enabled metallurgy. *Nat Commun* **2019,** *10* (1), 4645.

13 Li, Q.; Song, L.; Liang, Z.; Sun, M.; Wu, T.; Huang, B.; Luo, F.; Du, Y.; Yan, C.-H. A Review on CeO_2-Based Electrocatalyst and Photocatalyst in Energy Conversion. *Adv Energy and Sustainability Research* **2021,** *2* (2), 200063.

14 Li, Q.; Zeng, Z.; Sun, X.; Luo, F.; Du, Y. CeO_2 with diverse morphologies-supported IrO nanocatalysts for efficient oxygen evolution reaction - Commemorating the 100th anniversary of the birth of Academician Guangxian Xu. *J Rare Earths* **2021,** *39* (4), 357-363.

15 Kim, J.-H.; Shin, K.; Kawashima, K.; Youn, D. H.; Lin, J.; Hong, T. E.; Liu, Y.; Wygant, B. R.; Wang, J.; Henkelman, G.; Mullins, C. B. Enhanced Activity Promoted by CeO_x on a CoOx Electrocatalyst for the Oxygen Evolution Reaction. *ACS Catal* **2018,** *8* (5), 4257-4265.

16 Xu, H.; Wang, A.-L.; Tong, Y.-X.; Li, G.-R. Enhanced Catalytic Activity and Stability of Pt/CeO_2/PANI Hybrid Hollow Nanorod Arrays for Methanol Electro-oxidation. *ACS Catal* **2016,** *6* (8), 5198-5206.

17 Liu, Z.; Li, N.; Zhao, H.; Zhang, Y.; Huang, Y.; Yin, Z.; Du, Y. Regulating the active species of $Ni(OH)_2$ using CeO2:3D CeO_2/$Ni(OH)_2$/carbon foam as an efficient electrode for the oxygen evolution reaction. *Chem Sci* **2017,** *8* (4), 3211-3217.

18 Duan, Y. X.; Zhou, Y. T.; Yu, Z.; Liu, D. X.; Wen, Z.; Yan, J. M.; Jiang, Q. Boosting Production of HCOOH from CO_2 Electroreduction via Bi/CeO_x. *Angew Chem Int Ed Engl* **2021,** *60* (16), 8798-8802.

19 Valenti, G.; Melchionna, M.; Montini, T.; Boni, A.; Nasi, L.; Fonda, E.; Criado, A.; Zitolo, A.; Voci, S.; Bertoni, G.; Bonchio, M.; Fornasiero, P.; Paolucci, F.; Prato, M. Water-Mediated ElectroHydrogenation of CO_2 at Near-Equilibrium Potential by Carbon Nanotubes/Cerium Dioxide Nanohybrids. *ACS Appl Energy Mater* **2020,** *3* (9), 8509-8518.

20 Zheng, G.; Yan, J. M.; Yu, G. Nitrogen Reduction Reaction. *Small Methods* **2019,** *3* (6), 1900070

21 Xia, J.; Zhao, H.; Huang, B.; Xu, L.; Luo, M.; Wang, J.; Luo, F.; Du, Y.; Yan, C. H. Efficient Optimization of Electron/Oxygen Pathway by Constructing Ceria/Hydroxide Interface for Highly Active Oxygen Evolution Reaction. *Adv Funct Mater* **2020,** *30* (9).

22 Mukarakate, C.; Mittal, A.; Ciesielski, P. N.; Budhi, S.; Thompson, L.; Iisa, K.; Nimlos, M. R.; Donohoe, B. S. Influence of Crystal Allomorph and Crystallinity on the Products and Behavior of Cellulose during Fast Pyrolysis. *ACS Sustainable Chem & Eng* **2016,** *4* (9), 4662-4674.

23 Lv, C.; Yan, C.; Chen, G.; Ding, Y.; Sun, J.; Zhou, Y.; Yu, G. An Amorphous Noble-Metal-Free Electrocatalyst that Enables Nitrogen Fixation under Ambient Conditions. *Angew Chem Int Ed* **2018,** *57* (21), 6073-6076.

24 Tengyuan D, Xin Z, Mingzi S, Bolong H, Nan Z, Pengfei D, Rui Y, Zidong H, Wei W, Pinxian X, Chun-Hua Y. Uncovering the Promotion of CeO_2/$CoS_{1.97}$ Heterostructure with Specific

Spatial Architectures on Oxygen Evolution Reaction. *Adv Mater* **2021,** 2102593.

25 Liu, S.-Q.; Gao, M.-R.; Feng, R.-F.; Gong, L.; Zeng, H.; Luo, J.-L. Electronic Delocalization of Bismuth Oxide Induced by Sulfur Doping for Efficient CO_2 Electroreduction to Formate. *ACS Catal* **2021,** *11* (12), 7604-7612.

26 Deng, P.; Yang, F.; Wang, Z.; Chen, S.; Zhou, Y.; Zaman, S.; Xia, B. Y. Metal-Organic Framework-Derived Carbon Nanorods Encapsulating Bismuth Oxides for Rapid and Selective CO_2 Electroreduction to Formate. *Angew Chem Int Ed Engl* **2020,** *59* (27), 10807-10813.

27 Xu, L.; Zhao, H.; Sun, M.; Huang, B.; Wang, J.; Xia, J.; Li, N.; Yin, D.; Luo, M.; Luo, F.; Du, Y.; Yan, C. Oxygen Vacancies on Layered Niobic Acid That Weaken the Catalytic Conversion of Polysulfides in Lithium-Sulfur Batteries. *Angew Chem Int Ed* **2019,** *58* (33), 11491-11496.

28 Jin, X.; Duan, Y.; Liu, D.; Feng, X.; Li, W.; Zhang, Z.; Zhang, Y. CO Oxidation Catalyzed by Two-Dimensional Co_3O_4/CeO_2 Nanosheets. *ACS Appl Nano Mater* **2019,** *2* (9), 5769-5778.

29 Weixue W, Yang L, Yifan Y, Huihui W, Gong C, Chunyang G, Chunlin C, Yuejie A, Zhe C, Xiangke W. The Confined Interlayer Growth of Ultrathin Two-Dimensional Fe_3O_4 Nanosheets with Enriched Oxygen Vacancies for Peroxymonosulfate Activation. *ACS Catal* **2021,** 11, 11256−11265.

30 Hyung. S. K.; John. B. C.; Hao. L.; Jesse. S. K.; Sarah. H. T.; Vidvuds. O.; Bruce. D. Oxygen vacancies enhance pseudocapacitive charge storage properties of MoO_{3-x}. *Nat Mater* **2017,** 16, 454-460.

31 Xia, J.; Zhao, H.; Pan, W.; Yin, Z.; Zhou, B.; He, G.; Guo, Z.; Du, Y. Lanthanide doping induced electrochemical enhancement of $Na_2Ti_3O_7$ anodes for sodium-ion batteries. *Chem Sci* 2018, 9, 3421-3425.

32 Wang, Y.; Chen, Z.; Han, P.; Du, Y.; Gu, Z.; Xu, X.; Zheng, G. Single-Atomic Cu with Multiple Oxygen Vacancies on Ceria for Electrocatalytic CO_2 Reduction to CH_4. *ACS Catal* **2018,** *8* (8), 7113-7119.

33 Liu, H.; Xia, J.; Zhang, N.; Cheng, H.; Bi, W.; Zu, X.; Chu, W.; Wu, H.; Wu, C.; Xie, Y. Solid–liquid phase transition induced electrocatalytic switching from hydrogen evolution to highly selective CO_2 reduction. *Nat Catal* **2021,** *4* (3), 202-211.

34 S. J. Clark; M. D. Segall; C. J. Pickard; P. J. Hasnip; M. J. Probert; K. Refson; M. C. Payne, First Principles Methods Using Castep. *Zeitschrift Fur Kristallographie* **2005,** *220* (5-6), 567-570.

35 J. P. Perdew; K. Burke; M. Ernzerhof, Generalized Gradient Approximation Made Simple. *Phys Rev Lett* **1996,** *77* (18), 3865-3868.

36 P. J. Hasnip; C. J. Pickard, Electronic Energy Minimisation with Ultrasoft Pseudopotentials. *Comput Phys Commun* **2006,** *174* (1), 24-29.

37 J. P. Perdew; J. A. Chevary; S. H. Vosko; K. A. Jackson; M. R. Pederson; D. J. Singh; C. Fiolhais, Atoms, Molecules, Solids, and Surfaces: Applications of the Generalized Gradient Approximation for Exchange and Correlation. *Phys Rev B* **1992,** *46* (11), 6671-6687.

38 J. D. Head; M. C. Zerner, A Broyden-Fletcher-Goldfarb-Shanno Optimization Procedure for Molecular Geometries. *Chem Phys Lett* **1985,** *122* (3), 264-270.